Transitions between convective patterns in chemical fronts

Yunqing Wu,[1] Desiderio A. Vasquez,[2] Boyd F. Edwards,[1] and Joseph W. Wilder[3]
[1]*Department of Physics, West Virginia University, P.O. Box 6315, Morgantown, West Virginia 26506-6315*
[2]*Department of Physics, Indiana University-Purdue University Fort Wayne, Fort Wayne, Indiana 46805-1499*
[3]*Department of Mathematics, West Virginia University, P.O. Box 6310, Morgantown, West Virginia 26506-6310*
(Received 11 August 1995)

We present a theory for the transition from nonaxisymmetric to axisymmetric convection in iodate-arsenous acid reaction fronts propagating in a vertical slab. The transition takes place away from the onset of convection, where a convectionless flat front becomes unstable to a nonaxisymmetric convective front. The transition is studied by numerically solving a reaction-diffusion equation coupled with nonlinear hydrodynamics in a two-dimensional slab.

PACS number(s): 47.20.Bp, 47.70.Fw, 82.20.Mj

I. INTRODUCTION

The effects of convection on chemical wave propagation have been observed experimentally in several systems, including the iron-nitric acid reaction [1], the chlorite-thiosulfate reaction [2], the Belousov-Zhabotinsky reaction [3], and the iodate-arsenous acid reaction [4]. In these systems, convection enhances the chemical wave speed and affects the curvature of the front. Convection develops because of density gradients induced by either compositional or thermal gradients. Thermal effects are very important in systems that exhibit double-diffusive convection such as the iron-nitric acid system. For the iodate-arsenous acid reaction, the thermal length scale is large compared to the convective length scale, and the fluid can be considered as having uniform temperature, with convection being driven solely by the chemical gradient [5]. In this system, as the front propagates upward in capillary tubes, the front is flat, axisymmetric, or nonaxisymmetric, depending on the diameter of the tube.

A linear stability analysis for convectionless flat fronts showed that the transition to convection should be nonaxisymmetric in cylinders [6]. Nonlinear numerical studies near the onset of convection in a two-dimensional slab also obtained nonsymmetric convective fronts [7]. Experiments observe a transition to axisymmetric fronts. It was clear that to study axisymmetric fronts, the model had to be extended to regimes away from onset and a new numerical scheme was needed to detail with the long computations. In this paper we report such computations. We begin with an introduction to the basic equations governing the system. We then discuss the expansion method used to solve the two-dimensional Poisson equation and compared its performance with other, established methods. Our results are compared with previous linear and nonlinear analyses where appropriate. We relate our work to current experiments and suggest new experiments to test our results.

II. EQUATIONS OF MOTION AND LINEAR THEORY

Convectionless front propagation in the iodate-arsenous acid reaction with arsenous acid in stoichiometric excess can be described by a one-variable reaction-diffusion equation [8]:

$$\frac{\partial c}{\partial t}=D\nabla^2 c-\alpha c(c-c_2)(c-c_3)\ . \tag{1}$$

Here D is the molecular diffusivity, c is the iodide concentration ($[I^-]$), c_2 is the initial concentration of iodate ($[IO_3^-]$), and c_3 is the ratio of two reaction rate constants, $c_3=k_a/k_b$ and $\alpha=k_b[H^+]^2$. For the current calculation, we use the typical values $D=2.0\times10^{-5}$ $cm^2\,sec^{-1}$, $c_2=5.0\times10^{-3}$ M, $c_3=-1.0\times10^{-5}$ M, and $\alpha=3.45\times10^4$ $sec^{-1}M^{-1}$. With these parameters, the convectionless reaction-diffusion wave front has a constant speed of 0.029 mm/sec, typical of experiments.

To describe the effects of convective fluid motion, we couple the reaction-diffusion equation with the Navier-Stokes equation:

$$\frac{\partial \mathbf{V}}{\partial t}+(\mathbf{V}\cdot\nabla)\mathbf{V}=\frac{\rho-\rho_0}{\rho_0}\mathbf{g}-\frac{1}{\rho_0}\nabla P+\nu\nabla^2\mathbf{V}\ , \tag{2}$$

$$\nabla\cdot\mathbf{V}=0\ , \tag{3}$$

$$\frac{\partial c}{\partial t}+\mathbf{V}\cdot\nabla_c=D\nabla^2 c-\alpha c(c-c_2)(c-c_3)\ . \tag{4}$$

Here $\mathbf{V}$ is the fluid velocity, P is the reduced pressure related to the conventional pressure by $P=p-\rho_0 gz$, $g=-g\hat{z}$ is the acceleration of gravity ($g=980$ $cm\,sec^{-2}$) in the vertical ($-\hat{z}$) direction, $\nu=9.2\times10^{-3}$ $cm^2\,sec^{-1}$ is the kinematic viscosity, and ρ_0 is the density of the reacted fluid. Here we have used the Boussinesq approximation that includes the density difference only where it modifies the large gravity term [7]. In this paper, we only consider the density difference induced by the change in chemical concentration. Our previous work has shown that even though the reaction is exothermic and the density differences due to thermal expansion and chemical composition are comparable, the convective length scale is much smaller than the length scale of the temperature change [5], and thus thermal effects play a minor role. This allows us to neglect the heat equation by treating the temperature as uniform. Since the density differences are small, we assume a linear dependence of the density on

the iodide concentration c:

$$\rho=\rho_0[1-\beta(c-c_2)] . \quad (5)$$

Here, ρ_0 is the density of the reacted fluid. The coefficient of linear expansion ($\beta=1.7\times10^{-2}$ M^{-1}) is obtained from the experimental measurements of the isothermal fractional density difference $\delta=c_2\beta=0.84\times10^{-4}$ between the unreacted and reacted fluids, which measures the relative size of the small density differences.

A complete description of the experiments performed in test tubes requires a cylindrical geometry. To treat this geometry, we would have to solve the equations for a complicated nonlinear three-dimensional fluid flow. Instead we confine our attention to the two-dimensional slab and expect to obtain semiquantitative results for the transition between convective patterns above the onset of connection. In this case, the continuity equation [Eq. (3)] allows us to introduce a stream function ψ defined by the relations

$$V_x=\frac{\partial\psi}{\partial z} , \quad V_z=-\frac{\partial\psi}{\partial x} . \quad (6)$$

The vorticity ω is defined as

$$\omega=\nabla^2\psi , \quad (7)$$

and Eqs. (2) and (3) can be rewritten as

$$\frac{\partial\omega}{\partial t}=\frac{\partial(\psi,\omega)}{\partial(x,z)}+\beta g_z\frac{\partial c}{\partial x}+\nu\nabla^2\omega , \quad (8)$$

$$\frac{\partial c}{\partial t}=\frac{\partial(\psi,c)}{\partial(x,z)}+D\nabla^2c-\alpha(c-c_2)(c-c_3) . \quad (9)$$

Here we have defined

$$\frac{\partial(f_1,f_2)}{\partial(x,z)}=\frac{\partial f_1}{\partial x}\frac{\partial f_2}{\partial z}-\frac{\partial f_2}{\partial x}\frac{\partial f_1}{\partial z} . \quad (10)$$

We impose no-slip boundary conditions (vanishing fluid velocity) and no chemical flow at the walls. For an initial chemical concentration and fluid velocity, the evolution of the system is determined by Eqs. (7)–(9). This set of equations is highly nonlinear, requiring us to resort to numerical methods.

The linear stability analysis of the flat front was carried out by us previously [9]. We first considered a laterally unbounded front and introduced a small perturbation of fixed wavelength. We found that ascending flat fronts are unstable to perturbations of wavelengths greater than a critical wavelength. This explains the presence of convection in vertical capillary tubes of diameter larger than this critical wavelength. This linear stability analysis was carried out using a thin front approximation. In this limit, the reaction-diffusion equation is replaced by an eikonal relation between the normal velocity of the front C and its curvature κ:

$$C-\hat{\mathbf{n}}\cdot\mathbf{V}|_f=C_0-D\kappa . \quad (11)$$

Here C_0 is the flat front speed, $\mathbf{V}|_f$ is the fluid velocity at the reaction front, and $\hat{\mathbf{n}}$ is the unit vector perpendicular to the front pointing into the unreacted fluid. The second term on the left-hand side accounts for the effect of fluid motion. The eikonal relation provides the stability mechanism for the propagation of chemical fronts since it tends to lower the hills and raise the valleys. It is the competition between the stabilizing eikonal relation and the destabilizing fluid buoyancy that results in a stable convective curved front. A numerical linear stability analysis using the reaction-diffusion equation showed that the eikonal relation is an excellent approximation [10]. We also carried out a linear stability analysis on the two-dimensional slab and on the three-dimensional cylinder using no-slip boundary conditions [6,11]. We found that the dimensionless driving parameter

$$\mathcal{S}=\delta g d^3/\nu D \quad (12)$$

involving the cylinder radius d (or slab width d) and the corresponding fluid parameters completely determines the stability of planar fronts. This parameter measures the strength of buoyancy, which tends to destabilize a flat front in favor of convection, as opposed to curvature effects, which tend to flatten the front. This theory predicted that planar ascending fronts in vertical cylinders are unstable to nonaxisymmetric convection for $\mathcal{S}>\mathcal{S}_c=87.9$ and to axisymmetric convection for $\mathcal{S}>\mathcal{S}_s=370.2$. Similar calculations for the bounded slab gave the result of $\mathcal{S}_c=371.5$ and $\mathcal{S}_s=1805.5$ for antisymmetric and symmetric convection about the midplane, respectively. Using these critical values for $\mathcal{S}$ and the experimental values of the physical parameters, we calculated the critical slab widths for antisymmetric and symmetric instability: $d_c=0.929$ mm and $d_s=1.574$ mm. We will compare these results with our numerical simulations.

III. NUMERICAL METHOD

The system of Eqs. (7)–(9) was solved numerically in a two-dimensional vertical slab. The convectionless reaction-diffusion equation [Eq. (1)] can be solved efficiently by employing a rectangular grid on the spatial domain. The time evolution can be obtained with either an implicit or explicit Euler method. Once coupled to the Navier-Stokes equations, the difficulty of the numerical simulation lies in solving Eq. (7), which is a Poisson equation. The dynamics of the equation requires solving the Poisson equation as time evolves. A successive over-relaxation method proved to be too costly since it required several iterations to convergence for every time step. An improvement was found by using a cyclic reduction method. This method is used by the GENBUN subroutine of the FISHPAK package [12]. The number of operations per time step used by this method is proportional to $m*n*lg(n)$ for a mesh of size $m\times n$, where n is the number of grid points in the direction perpendicular to the wave propagation. In an effort to speed up our calculations, we developed a method based on a finite-mode truncation of the stream function, which has of the order $m*n*k$ operations per time step, where k is the number of basis functions used in the truncation. Evidently our finite-mode truncation method is good when the system can be accurately simulated by a small number of basis functions or when the grid number n is large. This

method runs at least three times faster than the GENBUN subroutine for our calculations with comparable accuracy. An additional advantage of this method is that the finite truncation makes use of symmetric and antisymmetric functions. This allows a better interpretation of the physical results based on the symmetry of the basis functions. This method is very useful in discovering the underlying patterns for this problem. We present here the details of the finite truncation method.

The chemical concentration c and the vorticity ω are obtained after a small time step using time evolution [Eqs. (8) and (9)]. Once the vorticity is obtained, the stream function ψ at the next time step is obtained by solving the Poisson equation defied by Eq. (7). Since we require no fluid velocity at the walls, the corresponding boundary conditions for the stream functions are $\psi=0$ and $\partial\psi/\partial z=0$ at the vertical walls. These boundary conditions can be satisfied by expanding the stream function in a series of complete orthonormal eigenfunctions of the operator d^4/dx^4:

$$\frac{d^4}{dx^4}\mathcal{T}_m=\lambda_m^4\mathcal{T}_m \ . \tag{13}$$

There are two classes of these functions: the even antisymmetric functions C_m and the odd symmetric functions S_m. Eigenvalues of and integrals over these functions are tabulated by Chandrasekar [13]. Accordingly, we approximate the stream function by a truncated expansion,

$$\psi(x,z,t)=\sum_{m=1}^{N} A_m(z,t)\mathcal{T}_m(x/d) \ , \tag{14}$$

where d is the wall separation. Truncating the series provides good approximation near the onset of convection, as shown in the linear stability analysis [11]. We also expect that this truncation will give good results even well above the onset, provided that the convective pattern is not too complicated. Away from the front in the vertical direction we require that the velocity field vanish, therefore imposing $\psi(x\rightarrow\pm\infty)\rightarrow 0$. This method can be modified to include other types of boundary conditions, such as free boundary conditions, or one free surface and one fixed wall, by choosing the appropriate basis functions in Eq. (14).

We project the vorticity and stream function onto T_n to eliminate the dependence on the x direction. Substituting Eq. (14) into Eq. (7), multiplying T_n on both sides of Eq. (14), and integrating over the slab width d, we obtain

$$(\omega|\mathcal{T}_n)=\frac{\partial^2}{\partial z^2}A_n(z,t)+\sum_m A_m(z,t)\left[\frac{d^2\mathcal{T}_m}{dx^2}\middle|\mathcal{T}_n\right] \ , \tag{15}$$

where

$$(f|\mathcal{T}_n)=\frac{1}{d}\int_{-d/2}^{+d/2} f(x)\mathcal{T}_n(x/d)dx$$

for a given $f(x)$. Furthermore, given the opposite parity of the functions S_m and C_m, the equations decouple into a set of equations for the coefficients $A_n(z,t)$ for even functions and another set for odd functions. For example, if we choose a four-term truncation including $C_1(x)$, $C_2(x)$, $S_1(x)$, and $S_2(x)$, we will have two sets of decoupled equations, each set containing two coupled equations. Projecting over $C_1(x)$ and $C_2(x)$ we have

$$f_1(z,t)=(\omega(x,z,t)|C_1(x))=\frac{d^2}{dz^2}A_1(z,t)-\frac{q_1^2}{d^2}A_1(z,t)-\frac{q_{12}^2}{d^2}A_2(z,t) \ ,$$

$$f_2(z,t)=(\omega(x,z,t)|C_2(x))=\frac{d^2}{dz^2}A_2(z,t)-\frac{q_{12}^2}{d^2}A_1(z,t)-\frac{q_2^2}{d^2}A_2(z,t) \ .$$

This system can be written by using a compact matrix notation as

$$\frac{d^2}{dz^2}\mathbf{A}-\frac{1}{d^2}\mathbf{Q}\,\mathbf{A}=\mathbf{f} \ . \tag{16}$$

Here we define $\mathbf{f}(z,t)=(f_m(z,t))=(\omega(x,z,t)|C_m(x))$, $\mathbf{A}(z,t)=(A_m(z,t))$, and $\mathbf{Q}=(q_{mn})=((d^2/dz^2)\times C_m(x)|C_n(x))$. The coefficients q_{mn} are tabulated in Ref. [14]. The linear system of coupled differential equations can be easily decoupled by transforming to a new basis generated by the eigenvectors of the coefficient matrix $\mathbf{Q}$:

$$\frac{d^2}{d^2z}\mathbf{A}'-\frac{1}{d^2}\mathbf{D}\,\mathbf{A}'=\mathbf{f}' \ . \tag{17}$$

Here $\mathbf{A}'=\lambda^{-1}\mathbf{A}$, $\mathbf{f}'=\lambda^{-1}\mathbf{f}$, $\mathbf{D}=\lambda^{-1}\mathbf{Q}\lambda$ is the diagonalized matrix of $\mathbf{Q}$, and λ is the eigenmatrix formed by the normalized eigenvectors of $\mathbf{Q}$. Once the equations are decoupled, the boundary value problem for the standard second order differential equation (16) can be solved either by Green's function method or with a forward-backward substitution [15]. We found the forward-backward substitution to be more efficient. To complete the solution of the Poisson equation we need to carry out a similar calculation using the odd functions $S_1(x)$ and $S_2(x)$. Once the coefficients $A_n(z,t)$ are computed, the stream function is obtained by substituting those coefficients into Eq. (14). This process is repeated successively for each time step.

In our numerical simulation, we use a flat chemical front solution plus small random perturbation near the front as our initial chemical concentration. All initial values of ψ and ω are set to zero. Because of the hydrodynamic instability, the fluid velocity gradually increases as the system evolves. It eventually becomes steady in a frame comoving with the chemical front. Our calculations were carried out using a four-term truncation as well as an eight-term truncation, depending on the parameter region. When the system is slightly above the onset of convection, the results obtained with a one-term truncation are not much different from those with a four-term truncation. Further above the onset of convection, the fluid velocity field becomes more complicated,

and more terms are required to ensure an accurate result. The accuracy of the truncation was guaranteed by analyzing the maximum value of the last term. In all of our calculations, the maximum value of the last coefficient included is less than 1% of the leading coefficient. This criterion is satisfied with a four-term truncation for widths $d < 2.0$ mm and with an eight-term truncation for widths $2.0 < d < 5.0$ mm. We have further checked a sample of our results by using the GENBUN subroutine, without observing any significant differences. The finite term truncation is faster than the GENBUN subroutine by a factor of 3.2 for the four-term and 2.3 for the eight-term truncation. The truncation also allows us to study the contributions of different modes to the fluid flow. It also helps in computing unstable and metastable states.

Our calculation use meshes of sizes 25×200, 40×300, and 50×400, depending on the slab width. In the horizontal direction the mesh size should not be too small in order to accurately represent the functions $S_m(x)$ and $C_m(x)$ over the mesh. At the same time, the spatial domain in the direction of propagation should be long enough to allow for the front to propagate and to reduce interactions with the upper and lower boundaries. We verify our selection of mesh size by doubling its size while keeping the physical space the same and comparing the results. In the experiments, the front propagates in a long tube without interacting with the ends of the tube. In the simulations the front is allowed to propagate a small distance and then it is shifted back to the center of the mesh, introducing unreacted steady fluid on the top of the slab to cover for the shift. This procedure is justified as long as the upper and lower boundaries are far away from the front.

IV. RESULTS

We investigate the onset of convection for chemical fronts ascending in a vertical slab of width d for the iodate-arsenous acid reaction. Our numerical results are summarized in Fig. 1, where the calculated ascending chemical wave speed v_f (filled circles) is plotted as a function of the slab width. The solid horizontal line in Fig. 1 represents the speed $v_f = 0.029$ mm/sec of the globally stable convectionless chemical wave. For $d \leq 0.92$ mm, the ascending wave has this speed. For slab widths between 0.92 and 2.75 mm the wave speed increases with the slab width. The slope decreases as the width approaches 2.75 mm but increases again as the width is further increased. The shape of the wave and the fluid flow also vary as a function of the slab width. For ascending waves in slabs of width $d \leq 0.92$ mm, the reaction front is flat, no fluid motion is present, and the chemical wave speed corresponds to the speed of the reaction-diffusion front. As the width increases beyond 0.92 mm, convection sets in and the speed of the chemical wave increases. For convective waves close to the onset of convection, the shape of the front is approximately antisymmetric, with a single convective roll traveling with the front, as shown in Fig. 2. In this region, fluid rises on one side of the slab and falls on the opposite side, resulting in a chemical front (solid trace) higher on one side and lower on the other. In Fig. 3 we show a chemical wave on a slab slightly below $d = 2.75$ mm. For this width ($d = 2.6$ mm), the fluid rises near the center of the slab and falls near the walls, leading to a chemical front higher near the center with two comoving convective rolls. However, one roll is stronger than the other, so the front is not quite symmetric. The region for rising fluid is wider than the region for falling fluid, but the velocity of the rising fluid is weaker compared to the velocity of the falling

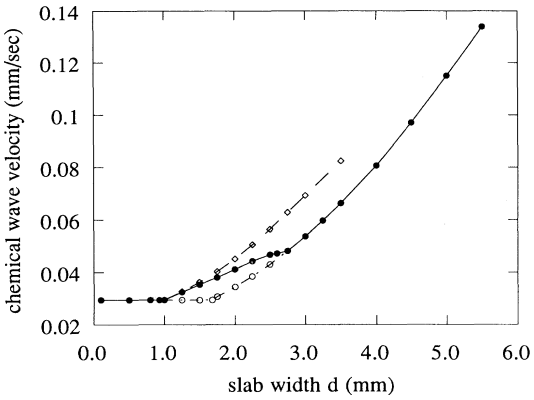

FIG. 1. Chemical wave speed as a function of the slab width d. Below the onset ($d < 0.92$ mm), chemical waves have a constant speed of 0.029 mm/sec. For widths 0.92 mm $\leq d \leq 0.275$ mm, the antisymmetric fronts and mixed states are observed. Above the second critical point ($d_s = 0.275$ mm), the chemical waves become completely symmetric. The solid line (●) represents the globally stable state. The dashed lines represent the unstable, purely antisymmetric state (◇) and the metastable purely symmetric state (○).

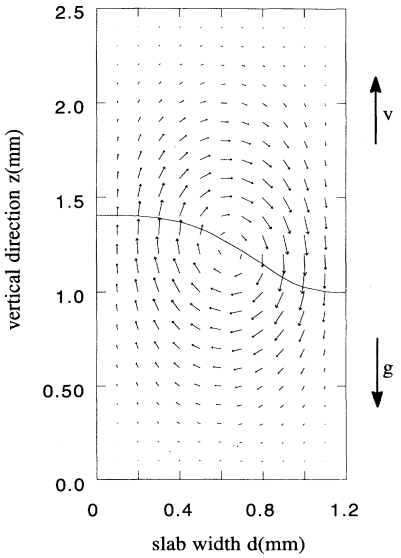

FIG. 2. Fluid velocity field and wave front shape for an ascending wave in a vertical slab of width $d = 1.2$ mm. The front is higher on one side than the other. A single convective roll is observed.

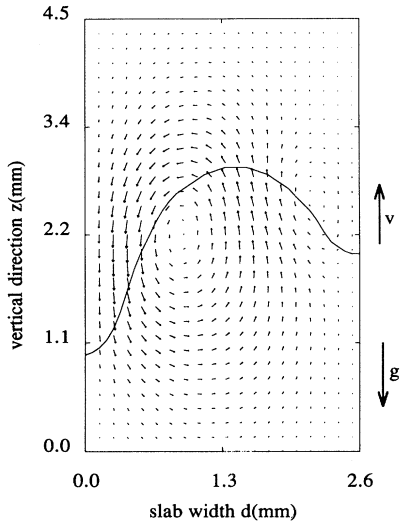

FIG. 3. Fluid velocity field and wave front shape for an ascending wave in a vertical slab of width $d=2.6$ mm. The fluid field is composed of both the antisymmetric modes and symmetric modes. A second convective roll can be seen near the right wall.

fluid. At this point, the system is close to the second critical point ($d_s=2.75$ mm) and close to becoming completely symmetric. Above d_s the front becomes completely symmetric, with the highest point of the front at the center of the slab (Fig. 4). There are two identical but counterotating convective rolls traveling with the front. The lighter reacted fluid rises at the center and the heavier unreacted fluid falls near the vertical walls, resulting in asymmetric front. As we further increase the width, the amplitude of the curved front increases and eventually becomes a long finger (Fig. 5), a symmetric wavefront with its length longer than its width. Our nonlinear calculations agree with the linear theory based on the eikonal relation [Eq. (11)]. The linear theory predicts the onset of convection near $d_c=0.92$ mm, which is consistent with our numerical results.

We show the evolution from a flat front to a steadily propagating curved front for $d=5.0$ mm in Fig. 6. Initially ($t=0$ min) the system is set to the convectionless flat front with a very small random perturbation near the front and no fluid flow. At $t=0.5$ min the front is still flat but the fluid velocity is growing because of the hydrodynamic instability. At this moment, the fluid motion is not strong enough to modify the shape of the front. At $t=1.5$ min, the front becomes roughly antisymmetric since the fastest growing antisymmetric unstable mode $C_1(x)$ dominates near the onset. Between $t=1.5$ min and $t=2.5$ min, both the antisymmeric and the symmetric modes grow and compete with each other. At first the antisymmetric modes are dominant. Latter the symmetric modes dominate. The sharp cusp at the left side of the front is due to the wave collision. At $t=3.5$ min, the wave becomes almost symmetric but is still evolving. At this moment, the left and the right sides of the front are not at the same height; consequently the front is not completely symmetric. At $t=4.5$ min and thereafter, the front is symmetric and propagates with a constant speed $v_f=0.115$ mm/sec. During the transient process the chemical wave speed is not well defined since the wave shape is constantly changing, with different local speeds at every part of the front. By averaging these local

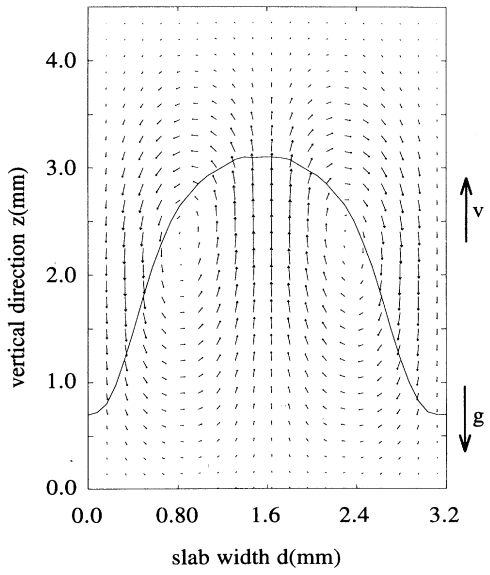

FIG. 4. Fluid velocity field and wave front shape for an ascending wave in a vertical slab of width $d=3.2$ mm. The front is completely symmetric, with the highest point at the slab center. The fluid field is composed only of symmetric modes and consists of two counterrotating rolls.

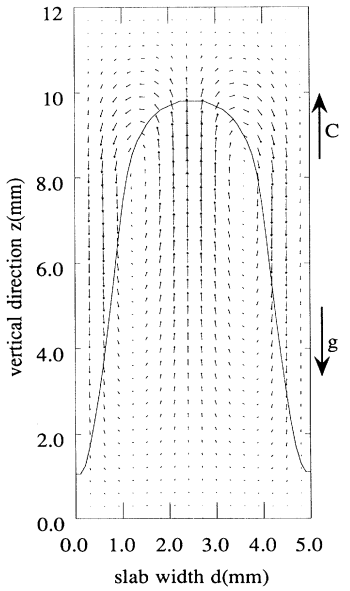

FIG. 5. Fluid velocity field and wave front shape for an ascending wave in a vertical slab of width $d=5.0$ mm. The propagating front has become a long finger.

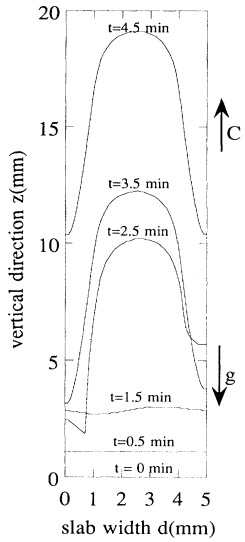

FIG. 6. Snapshots of the evolutionary process for the chemical front in the slab of width $d=5.0$ mm. The front is set initially to the convectionless flat front, with very small random perturbations. It first evolves into an antisymmetric front; later it goes through a mixed state and finally becomes a purely symmetric front.

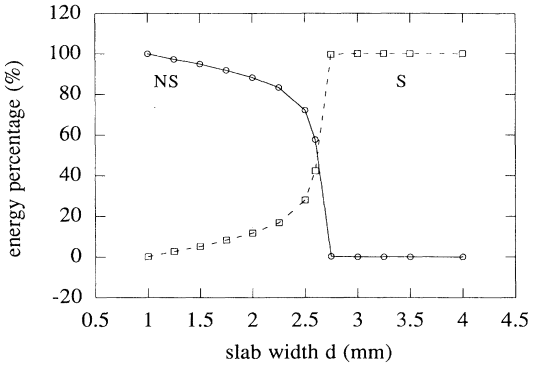

FIG. 7. Kinetic energy composition as a function of slab width d. The percentage of the kinetic energy from the antisymmetric modes (○) decreases, while the percentage of the symmetric modes (□) increases as the slab width increases. After d goes through a second critical point ($d_s=2.75$ mm) the flow is completely symmetric.

speeds, we observe a slow increase in average speed between $t=0-1$ min and a rapid increase after 1.0 min due to the fast growth of the antisymmetric modes. After that it gradually decreases to a constant value as the front becomes dominated by the symmetric modes. It is interesting to note that the temporal scenario of the system is similar to the scenario in parameter space. As time evolves, the system starts as a flat front; it later becomes antisymmetric, mixed, and then completely symmetric. This is the same scenario that we find in parameter space as we increase the slab width from zero to $d=5.0$ mm.

We study the transition from the antisymmetric state to the symmetric state by comparing the kinetic energy of the front with the energy of the pure symmetric and pure antisymmetric states. The pure antisymmetric state (diamonds in Fig. 1) is obtained by forcing the coefficients multiplying S_m to zero on the expansion, Eq. (14). The pure symmetric state (open circles in Fig. 1) is obtained in a similar way. This technique can be applied to our theoretical model, but it may not have an experimental counterpart. These states are obtained just to better understand the behavior at the different transitions. Because of the different parities and the orthogonality of the even and odd functions, we can decompose the total kinetic energy associated with convective fluid motion into the contributions of antisymmetric modes and symmetric modes. Purely antisymmetric solutions can be found only above $d=0.92$ mm; below that we find only flat fronts. These purely antisymmetric solutions have a higher chemical wave speed and higher kinetic energy associated with the convective fluid flow than the mixed state (Fig. 7). We test the stability of the antisymmetric solutions by using them as initial conditions for the full equations. The system then rapidly evolves into the stable mixed state. Thus we conclude that pure antisymmetric solutions are unstable. Purely symmetric solutions exhibit a different behavior when introduced into the full equations. Purely symmetric solutions can be found only for widths $d \geq 1.68$ mm. All symmetric solutions have lower chemical speed and lower kinetic energy associated with the convective fluid flow. We tested the stability of the symmetric state in the same way we tested the antisymmetric state. For symmetric fronts on slab widths between 1.68 and 2.75 mm, we find that, contrary to what happens to antisymmetric states, the solutions take a very long time to evolve into the mixed state. We therefore consider these symmetric solutions as metastable, in the sense that an initial symmetric state takes a very long time to decay into a mixed state (typically more than an hour in real time). Metastable states may be observed in experiments in a slab whose width decreases with increasing height. The wave should take a stable axisymmetric front in a slab with $d>2.75$ mm and keep its form for a period of an hour or even longer after propagated into the section where $d<2.75$ mm. For slab widths beyond 2.75 mm, the final steady state is purely symmetric, using either purely antisymmetric or purely symmetric solutions as initial conditions. It must be pointed out that a metastable purely symmetric solution within 1.68 mm $\leq d \leq 2.75$ mm has a symmetric front shape and a fluid velocity field similar to Fig. 4, except for having a smaller front amplitude. The unstable purely antisymmetric solutions for $d>0.92$ mm do not have an antisymmetric front shape, even though the velocity field is antisymmetric. This phenomenon can be understood by examining the symmetry of Eq. (4) under the transformation $x \rightarrow -x$. Only for symmetric velocity fields is the chemical concentration symmetric. For antisymmetric velocity fields, the chemical concentration does not have the similar symmetry.

As the slab width d increases, the symmetric modes contribute more and more to the total kinetic energy (Fig. 7). Near the onset of convection ($d_c=0.92$ mm) almost all of the kinetic energy is generated by the antisym-

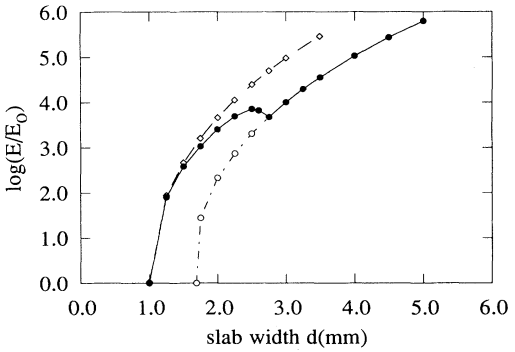

FIG. 8. The kinetic energy composition of the convective fluid motion. All unstable purely antisymmetric states (◇) have higher kinetic energy than the stable mixed states (●), while all metastable purely symmetric states (○) have lower kinetic energy than the mixed states. E_0 is the kinetic energy with $d=1.0$ mm. The base is $\log_{10}$.

metric components of the fluid flow. As d approaches the second critical point $d_s=2.75$ mm, the percentage of the symmetric modes contributing to the total kinetic energy rapidly increases to 100%. For mixed states (0.92 mm $\leq d \leq$ 2.75 mm), both components of fluid flow contribute to the kinetic energy. Mixed states have a kinetic energy higher than the purely symmetric state but lower than the purely antisymmetric state (Fig. 8).

Our results are consistent with experiments in cylinders. In experiments under the same conditions and parameters as we have used here Masere *et al.* [4] observed flat fronts for $d<1.1$ mm and nonaxisymmetric fronts in tubes of internal diameters 1.4 and 1.6 mm. Axisymmetric fronts are observed for tubes of internal diameters 2.3 mm and above. Because of different geometry, the critical points are different. Yet experiments show the same scenarios from flat fronts to nonaxisymmetric fronts and then to completely axisymmetric fronts as the diameter increases. Furthermore, the experiments also indicate changes in the slope of chemical wave speed vs diameter. Just above the onset of convection, the chemical wave speed increases as the diameter increases, but the slope decreases slightly near the second critical point. After the front becomes completely axisymmetric, the slope changes to an even larger number. This phenomenon is observable, but not so obvious, in the version of iodate-arsenous acid reaction with arsenous acid in stoichiometric excess, whereas this was dramatically shown in the other version of the experiment with that iodate excess [16], where the change of increase rate was very large compared with that near the saturation point.

V. CONCLUSIONS

By coupling the reaction-diffusion equations with the hydrodynamic equations, we observe the onset of convection and the transition between convective patterns from antisymmetric to completely symmetric convection. Associated with this transition we find abrupt changes in slope in the chemical wave speed versus slab width. We expect that the system will eventually evolve into a turbulent state, where there is no longer steady front propagation. To study the road to turbulence we need a more efficient scheme or idealized models.

Our simulations in a two-dimensional slab have shown a transition between patterns similar to the one observed in experiments in vertical cylinders. Even though the geometry is different, both cases allow fluid motion near the center of the fluid and no fluid motion near the walls because of the no-slip boundary conditions. The competition between the stabilizing curvature effect and the destabilizing buoyancy effect determines the critical point for convection. Above the onset, buoyancy and boundary conditions determine the possible convective pattern. The macroscopic convective fluid flow helps the intermixing of the reactive reagents and enhances the chemical front speed. The balance among the buoyancy, curvature, and fluid flow results in the steady propagation of the front. It would be interesting to simulate directly the chemical front propagation in the cylinder. This may be a complicated task because of the three-dimensionality of the flow and the singularity at the origin. We are currently working on a model based on a front evolution equation to treat the cylindrical problem.

ACKNOWLEDGMENTS

Helpful discussions with Jie Huang are gratefully acknowledged. This work is supported in part by the National Science Foundation Grant No. RII-8922106 and the National Research Center for Coal and Energy.

[1] G. Bazsa and I. R. Epstein, J. Phys. Chem. **89**, 3050 (1985); J. A. Pojman, I. P. Nagy, and I. R. Epstein, *ibid.* **95**, 1306 (1991).

[2] I. Nagypal, G. Bazsa, and I. R. Epstein, J. Am. Chem. Soc. **108**, 3635 (1986).

[3] H. Miike, S. C. Muller, and B. Hess, Chem. Phys. Lett. **144**, 515 (1988); Phys. Lett. A **141**, 25 (1989); Phys. Rev. Lett. **61**, 2109 (1988); H. Miike, H. Yamamoto, S. Kai, and S. C. Muller, Phys. Rev. E **48**, 1627 (1993).

[4] T. McManus, Ph.D thesis, West Virginia University, 1989 (unpublished); J. A. Pojman, I. R. Epstein, T. J. McManus, and K. Showalter, J. Phys. Chem. **95**, 1299 (1991); J. Masere, D. A. Vasquez, B. F. Edwards, J. W. Wilder, and K. Showalter, *ibid.* **98**, 6506 (1994).

[5] J. W. Wilder, B. F. Edwards, and D. A. Vasquez, Phys. Rev. A **45**, 2320 (1992); D. A. Vasquez, J. W. Wilder, and B. F. Edwards, Phys. Fluids, **7**, 2513 (1995).

[6] D. A. Vasquez, J. W. Wilder, and B. F. Edwards, Phys. Fluids A **4**, 2410 (1992).

[7] D. A. Vasquez, J. M. Littley, J. W. Wilder, and B. F. Edwards, Phys. Rev. E **50**, 280 (1994).

[8] A. Saul and K. Showalter, *Oscillations and Traveling Waves in Chemical Systems,* edited by R. J. Field and M. Burger (Wiley, New York, 1985).

[9] B. F. Edwards, J. W. Wilder, and K. Showalter, Phys. Rev. A **43**, 749 (1991).

[10] D. A. Vasquez, J. W. Wilder, and B. F. Edwards, J. Chem. Phys. **98**, 2138 (1993).

[11] D. A. Vasquez, B. F. Edwards, and J. W. Wilder, Phys. Rev. A **43**, 6694 (1991); D. A. Vasquez, J. Littley, B. F. Edwards, and J. W. Wilder, *ibid.* **47**, 1239 (1994).

[12] R. Sweet, SIAM J. No. Anal. **14**, 706 (1977); J. Adams, P. Swartztrauber, and R. Sweet, computer code FISHPAK, National Center for Atmospheric Research, Boulder, CO, 1980.

[13] S. Chandrasekar, *Hydrodynamic and Hydromagnetic Stability* (Oxford University Press, London, 1961), Appendix V.

[14] W. H. Reid and D. L. Harris, Astrophys. J. Suppl. Ser. **3**, 448 (1958).

[15] W. Press, B. Flannery, W. Vetterling, and S. Teukolsky, *Numerical Recipes in Fortran,* 2nd ed. (Cambridge University Press, Cambridge, 1992), Chap. 2.

[16] J. Masere (private communication).